JOINT EUROPEAN TORUS

JET–P(92)35

H. Bindslev
and JET Team

Relativistic Effects in Plasma Reflectometry

Relativistic Effects in Plasma Reflectometry

H. Bindslev and JET Team*

JET-Joint Undertaking, Culham Science Centre, OX14 3DB, Abingdon, UK

Risø National Laboratory, Roskilde, Denmark
** See Annex*

Preprint of Paper to be submitted for publication in
Plasma Physics and Controlled Fusion

Relativistic Effects in Plasma Reflectometry

H. Bindslev*
JET Joint Undertaking, Abingdon, Oxon, OX14 3EA, UK.

29 June 1992

Abstract

The refractive indices and the cutoff conditions for electromagnetic waves in plasmas are investigated for cold, hot and relativistic plasma models. Significant relativistic modifications of refractive indices and locations of cutoffs are found in regimes relevant for reflectometry in large Tokamaks. For X–mode it is demonstrated that these effects may shift the location of the reflecting layer by a significant fraction of the minor radius and that the cold model may lead to considerable underestimations of the density profile. Relativistic effects predicted for O–mode reflectometry are smaller than for X–mode, but not negligible. An algorithm for reconstruction of density profiles which allows a relativistic plasma model to be used is presented.

1 Introduction

In Tokamaks and other plasma devices reflectometry is proving to be a useful method for diagnosing the electron density [COSTLEY, 1991]. Broad band and multichannel narrow band reflectometry have become reliable means of diagnosing the electron density profile [PRENTICE, 1990; DOYLE, 1990; MANSO, 1991; SIPS 1991], while correlation reflectometry offers the possibility of localized measurement of density fluctuations [CRIPWELL, 1989; MAZZUCATO, 1991; ZOU, 1991; CRIPWELL, 1991]. Dual mode reflectometry may provide a means of measuring the magnetic field profile [PAVLICHENKO, 1989; COSTLEY, 1990]. All these applications rely on measurements of the phase change which a probing beam undergoes while propagating from a launching antenna, through the plasma to a reflecting layer at a cutoff and back to a receiving antenna.

Although electron temperatures found in large tokamaks (5–15 keV) remain small relative to the rest mass energy of the electrons (511 keV), recent investigations have revealed significant relativistic shifts in the locations of cutoffs and modifications of the refractive index in the regions leading up to these cutoffs [BATCHELOR *et al.*, 1984; BINDSLEV, 1991 a, b and c]. This is caused partly by the fact that the refractive index in the vicinity of a cutoff is quite sensitive to the plasma response. It is, however, also found that the relativistic modifications of the Hermitian part of the dielectric tensor are larger than would be expected from a straightforward comparison of the electron temperature with the electron rest mass energy.

*Permanent address: Risø National Laboratory, DK–4000 Roskilde, Denmark.

This paper investigates the relativistic modifications of the dispersion in a plasma in the regimes which are relevant for reflectometry, and explores the consequences these modifications have on the interpretation of reflectometry data. Methods for analyzing reflectometry data with a relativistic plasma model are given.

The paper is organized as follows. In section 2 the *relativistic* plasma model is outlined and a computationally convenient expression for the *weakly relativistic* dielectric tensor (due to SHKAROFSKY, 1986) is given. Section 3 presents numerical evaluations of the refractive indices for ordinary mode (O–mode) and extraordinary mode (X–mode) propagation based on the *cold*, the *hot* and the *weakly relativistic* plasma models. In section 4 numerical evaluations of a number of quantities relating to the *fully relativistic* O–mode cutoff and X–mode R cutoff are presented, including the locations of the relativistic cutoffs in an ω_c/ω versus ω_p^2/ω^2 diagram (CMA diagram). A general algorithm for reconstruction of electron density profiles from reflectometry data is derived in section 5. In section 6 simulated broad band reflectometry data are analysed with the cold and the weakly relativistic models. Consequences for existing and possible future diagnostics are discussed. Section 7 summarizes the findings in this paper.

2 Relativistic plasma model

The *cold* plasma model is well known. In this paper the *hot* plasma model refers to a magnetized plasma with an isotropic Maxwellian velocity distribution for the electrons. In the hot model the dielectric tensor, ϵ, is derived from Maxwell's equations and the non–relativistic Vlasov equation (see eg. SWANSON, 1989).

In the *relativistic* model the constitutive equations are

$$\mathbf{J} = \sum_j n_j q_j \int \mathbf{v}_j \, f_j(\mathbf{p}) \, d\mathbf{p} \,, \tag{1}$$

$$\frac{\partial f}{\partial t} + \mathbf{v} \cdot \frac{\partial f}{\partial \mathbf{r}} + q(\mathbf{E} + \mathbf{v} \times \mathbf{B}) \cdot \frac{\partial f}{\partial \mathbf{p}} = 0 \tag{2}$$

where $\mathbf{v} = \mathbf{p}/\gamma m$ and $\gamma = \sqrt{1 + (p/mc)^2}$. The unperturbed velocity distribution corresponding to thermodynamic equilibrium is

$$f^0 = \frac{\alpha \exp(-\alpha\gamma)}{4\pi(mc)^3 K_2(\alpha)} \quad , \qquad \alpha = \frac{m_e c^2}{T_e} \,. \tag{3}$$

K_n is the modified Bessel function of the second kind and order n.

The relativistic dielectric tensor is derived from Maxwell's equations with the plasma current response described by equations (1), (2) and (3). Various expressions for the fully relativistic dielectric tensor have been derived [TRUBNIKOV, 1959; BORNATICI, 1983].

Fully relativistic expressions for ϵ are generally difficult to handle numerically. A much more tractable form known as the *weakly relativistic* dielectric tensor, derived from TRUBNIKOV's

result by SHKAROFSKY (1986), is given below. It is valid for $\alpha \gg 1$ and $\lambda < 1$ (λ is defined below) and is a very good approximation at the temperatures found in large Tokamaks.

$$\epsilon_{ij} = \mathbf{I} - \frac{\alpha\omega_p^2}{\omega^2} \sum_{N=-\infty}^{\infty} \sum_{p=0}^{\infty} a_{pn} \lambda^{p+n-1} M_{ij} \quad , \qquad \lambda = \left(\frac{k_\perp v_t}{\omega_c}\right)^2 , \; v_t = \sqrt{\frac{T_e}{m_e}} , \tag{4}$$

$$\mathbf{M} = \left\{ \begin{array}{ccc} n^2 \mathcal{F}_{p+n+3/2} & -iN(p+n)\mathcal{F}_{p+n+3/2} & \frac{k_\perp k_\parallel c^2}{\omega\omega_c} N \mathcal{F}'_{p+n+5/2} \\ -M_{12} & \left[(p+n)^2 - \frac{p(p+2n)}{2n+2p-1}\right] \mathcal{F}_{p+n+3/2} & \frac{ik_\perp k_\parallel c^2}{\omega\omega_c}(p+n)\mathcal{F}'_{p+n+5/2} \\ M_{13} & -M_{23} & \lambda(\mathcal{F}_{p+n+5/2} + 2\psi^2 \mathcal{F}''_{p+n+7/2}) \end{array} \right\} ,$$

$$a_{pn} = \frac{(-1)^p (n+p-1/2)!}{p!(n+p/2)!(n+(p-1)/2)!2^n} \quad , \qquad n = |N| \quad ,$$

$$\mathcal{F}_q = -i \exp(-\psi^2) \int_0^\infty (1-it)^{-q} \exp[-i\phi^2 t + \psi^2/(1-it)]\, dt \quad ,$$

$$\mathcal{F}^m = \frac{\partial^m \mathcal{F}}{\partial(\phi^2)^m} \quad , \qquad \psi = \frac{k_\parallel c^2}{\sqrt{2}\omega v_t} \quad , \qquad \phi^2 = \psi^2 - \alpha\left(\frac{\omega - N\omega_c}{\omega}\right).$$

The coordinate system is oriented such that $\hat{\mathbf{z}}$ is in the direction of the magnetic field, $\mathbf{B}$, and the wave vector, $\mathbf{k}$, lies in the x–z plane. The required Shkarofsky functions, $\mathcal{F}_q^m(\phi, \psi = 0)$, are readily evaluated by the use of recursion relations and expressions relating the lower order functions to the Fried and Conte dispersion function [SHKAROFSKY, 1986].

For the conditions investigated in this paper the summation over powers of λ in expression (4) converges rapidly. For these conditions λ is typically smaller than $5 \cdot 10^{-2}$ and it is generally sufficient to include only terms up to the fifth power in λ.

3 Refractive index

Electromagnetic waves in a homogeneous source–free plasma satisfy the homogeneous wave equation

$$\begin{aligned} \mathbf{\Lambda E} &= 0, \qquad (5) \\ \mathbf{\Lambda}(\mathbf{k},\omega) &= \boldsymbol{\epsilon}(\mathbf{k},\omega) + \mu^2\{\hat{\mathbf{k}}\hat{\mathbf{k}} - \mathbf{I}\}, \end{aligned}$$

where μ is the refractive index, ω the angular frequency, $\mathbf{k}$ the wave vector, $\hat{\mathbf{k}}$ the unit wave vector and $\mathbf{I}$ the identity tensor. Non-trivial solutions to (5) only exist if

$$\Lambda = |\Lambda| = 0. \tag{6}$$

This is the dispersion equation. In a cold plasma an explicit expression for μ can be derived by solving for μ in (6). In hot and relativistic plasmas, where ϵ is a function of μ, (6) is a transcendental equation in μ. In this case the refractive indices of the modes of the plasma are found numerically by searching for the roots of Λ in the complex μ plane. Whereas in the cold plasma at most 3 modes exist, in the hot and relativistic plasmas there are in general an infinity of modes, though most of them are heavily damped. A typical situation at frequencies above the R cutoff is illustrated in figure 1.

Cold, hot and weakly relativistic calculations of the O-mode refractive index as a function of density at $f = 30$, 60 GHz and $T_e = 10$ keV are presented in figures 2 (a) and (b). The cold and the hot curves are indistinguishable.

In Tokamaks, X-mode reflectometry makes use of waves with frequencies between the 1^{st} and 2^{nd} harmonics of the electron cyclotron frequency and above the R cutoff frequency. Calculations of the refractive index in this region are presented in figures 2 (c)-(f). Cold, hot and weakly relativistic calculations for $T_e = 10$ keV and $f = 100$, 110 and 120 GHz are compared in figures 2 (c)-(e). While the hot model produces only a small change relative to the cold model and tends towards the cold model at the R cutoff, the weakly relativistic model predicts a substantial change in the refractive index and the density of the R cutoff is increased considerably. In figure 2 (f) the refractive index is calculated relativistically for four different temperatures to display the temperature dependence of the relativistic effects. The $T_e = 0.05$ keV curve is indistinguishable from the cold curve.

It is noteworthy that the relativistic effects are more important than the effects found with the hot model in all the regimes explored here. The following analysis will therefore only be concerned with the cold and relativistic models.

4 Cutoffs

The locations of the O-mode cutoff and the X-mode R cutoff predicted by a fully relativistic model are given by [BATCHELOR *et al.*, 1984; BINDSLEV, 1991 a]

$$\left(\frac{\omega_p^2}{\omega^2}\right)_{\text{O cutoff}} = \nu_O = \frac{3K_2(\alpha)}{\alpha^2 \int_0^\infty (p^4/\gamma^2) e^{-\alpha\gamma}\, dp}\ , \tag{7}$$

$$\left(\frac{\omega_p^2}{\omega^2}\right)_{\text{R cutoff}} = \nu_R = \frac{3K_2(\alpha)}{\alpha^2 \int_0^\infty \left(1 + \frac{\omega_{ce}/\omega}{\gamma}\right) \frac{p^4 e^{-\alpha\gamma}}{\gamma^2 - (\omega_{ce}/\omega)^2}\, dp}\ , \tag{8}$$

where K_2 is the modified Bessel function of the second kind and order 2.

The locations of cutoffs found with the weakly relativistic code agree accurately with the results found with the fully relativistic expressions (7) and (8). In figure 3 the locations of the O–mode cutoff and the X–mode R cutoff predicted by the fully relativistic model (equations (7) and (8)) are plotted in an ω_c/ω versus ω_p^2/ω^2 diagram (CMA diagram) for T_e = 0.1, 5, 10, 15, 20 keV.

As may be seen in figures 2 and 3, the largest *relative* shift occurs for the R cutoff near the cyclotron frequency. Relativistic effects in reflectometry should therefore be most noticeable in this region.

Relativistic effects increase the density at which a wave is cut off in both O–mode and X–mode. Cutoff densities calculated with equations (8) and (7) and normalized by the equivalent cutoff densities found with the cold theory,

$$\left(\frac{n_{e\,\mathrm{rel}}}{n_{e\,\mathrm{cold}}}\right)_{\mathrm{O\ cutoff}} = \nu_O\ , \tag{9}$$

$$\left(\frac{n_{e\,\mathrm{rel}}}{n_{e\,\mathrm{cold}}}\right)_{\mathrm{R\ cutoff}} = \frac{\nu_R}{1-\omega_c/\omega}\ , \tag{10}$$

are plotted as functions of temperature in figure 4.

In X–mode the temperature dependence of the cutoff density varies with ω_c/ω. Curves are given for O–mode and for X–mode with a range of values of ω_c/ω.

Expanding (7) to third power in T_e provides a simple expression for the normalized O–mode cutoff density which is accurate to five significant digits at temperatures below 20 keV:

$$\nu_O \approx 1 + 4.892\cdot 10^{-3}\left(\frac{T_e}{\mathrm{keV}}\right) - 2.24\cdot 10^{-6}\left(\frac{T_e}{\mathrm{keV}}\right)^2 + 2.3\cdot 10^{-8}\left(\frac{T_e}{\mathrm{keV}}\right)^3\ . \tag{11}$$

A simple approximation to the relativistic refractive index for O–mode radiation propagating perpendicular to B is given by

$$\mu_O \approx \sqrt{1-\frac{\omega_p^2}{\nu_O\omega^2}}\ . \tag{12}$$

At temperatures below 20 keV expression (12) with ν_O given by (11) is generally accurate to two or more significant digits, and typically accurate to four significant digits in the region near the cutoff.

To explore the consequences of the relativistic modifications for reflectometry, plasmas are assumed to have the following profiles of electron density, n_e, electron temperature, T_e, and magnetic field, B:

$$n_e = (n_{e0} - n_{el})\left(1 - (r/a)^2\right)^{p_n} + n_{el} \quad (13)$$

$$T_e = (T_{e0} - T_{el})\left(1 - (r/a)^2\right)^{p_T} + T_{el} \quad (14)$$

$$B = (B_0 R_0)/(R_0 + r) \quad (15)$$

Cutoff frequencies calculated on the basis of equations (7) and (8) as functions of major radius are given in figures 5 (a)–(c) for a range of central temperatures, T_{e0}, and values of density and magnetic field which are typical of JET plasmas. It is clear that in both modes the cutoff point may, in the central region, be shifted by a significant fraction of the minor radius.

5 General algorithm for density profile reconstruction

It is evident that the relativistic modification of the refractive index and in particular the shift of the cutoff density will change the relation between the density profile and the phase change which a probing wave undergoes in the plasma. An algorithm for reconstruction of the density profile from reflectometric data which is valid for both O–mode and X–mode in the relativistic model is therefore required. One such algorithm is derived here. It is of course also valid for the cold model.

It is assumed that the phase shift which the probing wave undergoes in the plasma is $2(\omega/c)\Psi(\omega) - \pi/2$ where ω is the frequency of the probing wave, c is the speed of light and $\Psi(\omega)$ is the optical distance from the plasma edge to the cutoff layer [GINZBURG, 1970],

$$\Psi(\omega) = \int_{r_{\text{cutoff}}(\omega)}^{a} \mu \, dr \, . \quad (16)$$

ϵ is analytic in μ^2 at $\mu = 0$ (cf. equation (4)). From this it follows that Λ is analytic in μ^2 at $\mu = 0$ and hence

$$\frac{\partial \Lambda}{\partial \mu} = 2\mu \partial \Lambda / \partial \mu^2 = 0 \text{ at } \mu = 0, \quad (17)$$

while in general

$$\frac{\partial \Lambda}{\partial \mu^2} \neq 0 \text{ at } \mu = 0. \quad (18)$$

Since Λ is analytic in X, where X equals B, n_e or T_e (cf. equation (4)), it follows from (18) that

$$\frac{\partial \mu^2}{\partial X} = \frac{-\partial \Lambda / \partial X}{\partial \Lambda / \partial \mu^2} \quad (19)$$

tends to a finite limit as $\mu \to 0$, while

$$\frac{\partial \mu}{\partial X} = \frac{-\partial \Lambda / \partial X}{\partial \Lambda / \partial \mu} \tag{20}$$

does not.

Let $\mu(x)$ be the refractive index at the distance x from the cutoff. Expanding $\mu^2(x)$ around the cutoff we get to lowest order in x

$$\mu^2(x) = \left(\frac{\partial \mu^2}{\partial B}\frac{\partial B}{\partial x} + \frac{\partial \mu^2}{\partial n_e}\frac{\partial n_e}{\partial x} + \frac{\partial \mu^2}{\partial T_e}\frac{\partial T_e}{\partial x} \right) x \, . \tag{21}$$

Let $\delta\Psi$ be the integral of μ from the cutoff out to a distance Δ

$$\delta\Psi = \int_0^\Delta \mu(x)\, dx = \sqrt{\frac{\partial \mu^2}{\partial B}\frac{\partial B}{\partial x} + \frac{\partial \mu^2}{\partial n_e}\frac{\partial n_e}{\partial x} + \frac{\partial \mu^2}{\partial T_e}\frac{\partial T_e}{\partial x}}\ \frac{2}{3}\Delta^{3/2}. \tag{22}$$

The second equality is valid to lowest order in Δ. From equations (21) and (22) we get an expression for $\partial n_e/\partial x$ in the vicinity of the cutoff which together with the expression for Δ, implicit in (21), forms the basis for the inversion algorithm:

$$\frac{\partial n_e}{\partial r} = \left(\frac{2\mu^3}{3\delta\Psi} - \frac{\partial \mu^2}{\partial B}\frac{\partial B}{\partial r} - \frac{\partial \mu^2}{\partial T_e}\frac{\partial T_e}{\partial r} \right) \Big/ \frac{\partial \mu^2}{\partial n_e} \tag{23}$$

$$\Delta = \frac{3\delta\Psi}{2\mu} \, . \tag{24}$$

In equations (23) and (24) μ is the refractive index at the distance Δ from the cutoff while the gradients, which vary slowly, can be evaluated anywhere in the vicinity of the cutoff. The assumptions about analyticity made in the derivation clearly also hold for the cold model.

Given the spatial profiles of the magnetic field and of the temperature, an iterative procedure for reconstructing the density profiles is readily derived from expressions (23) and (24). Assume that experimental data on the phase shift function are available at discrete frequencies, ω_i. Waves at these frequencies are cut off at points, r_i, with densities n_i. Further assume that the density profile has been reconstructed from the edge to the $(i-1)$th cutoff point, using the experimental data at frequencies up to and including the $(i-1)$th frequency. The distance from r_{i-1} to r_i can then be estimated with expression (24) where $\delta\Psi$ is obtained from the experimental data at frequency ω_i and that part of the density profile which has already been reconstructed. The density at the ith cutoff point can be estimated with expression (23). The explicit form of this iterative algorithm is

$$r_0 = a \tag{25a}$$

$$\bar{n}_0 = n_{e\,\mathrm{cutoff}}(\omega_0, B_0, T_0)\,; \quad B_{i-1} = B(r_{i-1})\,;\; T_{i-1} = T_e(r_{i-1}) \tag{25b}$$

$$\omega_i = \omega_0 + i\delta\omega \tag{25c}$$

$$(\mu^2)_i = \mu^2(\omega_i, \bar{n}_{i-1}, B_{i-1}, T_{i-1}) \tag{25d}$$

$$\left(\frac{\partial\mu^2}{\partial X}\right)_i = \left(\frac{\partial\mu^2}{\partial X}\right)(\omega_i, \bar{n}_{i-1}, B_{i-1}, T_{i-1})\,; \quad X = n_e, B, T_e \tag{25e}$$

$$\bar{\Psi}_i = \int_{r_{i-1}}^{a} \bar{\mu}(\omega_i, r)\, dr \quad ; \qquad \bar{\mu}(\omega_i, r_j) = \mu(\omega_i, \bar{n}_j, B_j, T_j) \tag{25f}$$

$$\delta\Psi_i = \Psi_i - \bar{\Psi}_i \quad ; \qquad \Psi_i = \int_{r_{\mathrm{cutoff}}(\omega_i)}^{a} \mu_{\mathrm{rel}}(\omega_i, r)\, dr \tag{25g}$$

$$\left(\frac{\partial\bar{n}}{\partial r}\right)_i = \left(\frac{(2\mu^3)_i}{3\delta\Psi_i} - \left(\frac{\partial\mu^2}{\partial B}\right)_i \frac{\partial B(r_{i-1})}{\partial r} - \left(\frac{\partial\mu^2}{\partial T_e}\right)_i \frac{\partial T(r_{i-1})}{\partial r}\right) \Bigg/ \left(\frac{\partial\mu^2}{\partial n_e}\right)_i \tag{25h}$$

$$\Delta_i = \frac{3\delta\Psi_i}{2\mu_i} \tag{25i}$$

$$r_i = r_{i-1} - \Delta_i \tag{25j}$$

$$\bar{n}_i = \bar{n}_{i-1} - \left(\frac{\partial\bar{n}}{\partial r}\right)_i \Delta_i \quad . \tag{25k}$$

$\bar{n}_i$ is the reconstructed electron density at the minor radius r_i (r_i is negative on the inside of the plasma). Having determined r_i the density, $\bar{n}_i$, could of course also be determined from equation (7) or (8), or the equivalent cold equation. This provides a convenient means of checking the reconstruction.

If the group delay time,

$$\tau = \frac{2\omega}{c}\left(\frac{\partial\Psi}{\partial\omega}\right)\,, \tag{26}$$

is available instead of the phase function then expressions (25f) and (25g) in the algorithm are replaced by

$$\delta\Psi_i = (\omega_i - \omega_{i-1})\left(\frac{\partial\Psi}{\partial\omega}\right)_i - \int_{r_{i-1}}^{a} (\bar{\mu}(\omega_i, r) - \bar{\mu}(\omega_{i-1}, r))\, dr\,. \tag{27}$$

6 Reconstruction of density profiles from simulated data

To simulate reflectometric data the phase function $\Psi(\omega)$, as given in equation (16), was calculated relativistically for a range of plasmas with profiles given by equations (13)–(15). Density profiles were then reconstructed from $\Psi(\omega)$ with the algorithm given above using the cold and the relativistic plasma model.

The reconstructed density profiles are identical to the actual density profiles when the reconstruction is based on the relativistic plasma model. This demonstrates that the above algorithm is numerically stable and accurate, and that reconstruction based on a relativistic plasma model is feasible.

For O–mode reflectometry, reconstruction based on the simple approximation to the relativistic refractive index, given in equations (11) and (12), also results in accurately reconstructed density profiles. For the parameters used in figure 6 (a) the reconstructed profiles, obtained with this simple approximation, were all accurate to three or more significant digits.

When the reconstruction is based on the cold plasma model the reconstructed density profiles underestimate the actual density profiles, by a considerable amount in X–mode and by a smaller, though still significant, amount in O–mode. Examples of density profiles reconstructed with the cold model are given in figures 6 (a)–(c), 7 and 8.

The plasma parameters used for the calculations presented in figures 6 (a)–(c) are typical of JET plasmas and identical to those used for the graphs in figures 5. Figure 6 (a) shows reconstructed density profiles obtained for O–mode.

To judge the significance of the relativistic effects for the JET O–mode multichannel reflectometer [PRENTICE, 1990] the relativistic shifts of profiles are compared with the errors that enter the measurement from other sources. To this end it is convenient to separate the density profile into three zones: the edge with very steep gradients ($\frac{\partial n}{\partial r}/n \gg 1/a$); the confinement region with moderate gradients ($\frac{\partial n}{\partial r}/n \approx 1/a$) and densities which are significant fractions of the peak density; and the central region with small gradients ($\frac{\partial n}{\partial r}/n \ll 1/a$).

Errors not related to relativistic effects manifest themselves as an uncertainty in the radial location of the cutoff point associated with a given frequency. The cutoff density associated with a frequency is not changed by these errors. Non–relativistic errors in the density profile are therefore conveniently expressed in terms of radial uncertainties. The profile shifts caused by relativistic effects are mainly due to changes in cutoff density associated with a given frequency, though shifts in the location of the cutoff point do also contribute. For the purpose of this comparison it is helpful, in the regions with non–vanishing density gradients, to think of the relativistic shifts in terms of radial displacements.

At the edge the errors from non–relativistic sources can be brought down to about 4 cm [SIPS, 1992]. The relativistic shift at the edge is negligible because the temperature is low and even if it is not, the relativistic effects do not shift the radial location of a sufficiently high step in density. Only the height of the step and the densities on either side of the step would be affected.

In the confinement region the non–relativistic errors can be brought down to 6 cm or less

[SIPS, 1992]. This is comparable to the relativistic shifts and it appears that under some conditions the relativistic effects could be the dominant source of errors in this region.

In the central region the non–relativistic errors become very large and details of the profile are seldom available here. It is however possible to give accurate information about the peak density at the points in time when a channel changes from reflection to transmission or the reverse. The non–relativistic errors on these data are negligible. Correcting for the relativistic effects increases the predicted peak density by typically 5 to 8 % depending on the temperature (see figure 4 and equations (9) and (11)).

It must be concluded that a data analysis which takes the relativistic effects into account is likely to improve significantly the accuracy of the JET O–mode multichannel reflectometer. The codes for analyzing data from this diagnostic will therefore be updated in the near future to take relativistic effects into account.

Figures 6 (b) and (c) show reconstructed density profiles obtained from X–mode. An X–mode reflectometer for profile measurements at JET would clearly require a relativistic data analysis. The relativistic effects in X–mode reflectometry are so large that they will not be masked by non–relativistic errors in the measurements, provided the non–relativistic errors are small enough to allow useful profile data to be obtained from X–mode in the first place.

To estimate the relativistic effects at various values of n_{e0} and B_0 it is useful to note that the graphs of the reconstructed densities normalized by n_{e0} are invariant under changes of n_{e0} and B_0 which keep n_{e0}/B_0^2 constant:

$$\frac{\bar{n}(r)}{n_{e0}} = \bar{\mathrm{N}}\left\{\eta, \frac{n_e(r)}{n_{e0}}, \frac{B(r)}{B_0}, T_e(r)\right\} . \tag{28}$$

$\bar{\mathrm{N}}$ is the operator representing the relation between the reconstructed density, $\bar{n}(r)$, and the actual plasma parameters. η is a convenient dimensionless parameter which is proportional to n_{e0}/B_0^2:

$$\eta = \frac{\omega_{p0}^2}{\omega_{c0}^2} = \frac{m_e}{\varepsilon_0}\frac{n_{e0}}{B_0^2} = 1.029\frac{n_{e0}/10^{19}\mathrm{m}^{-3}}{(B_0/\mathrm{T})^2} . \tag{29}$$

The invariance of $\bar{n}(r)/n_{e0}$ under changes in plasma parameters which leave η, $n_e(r)/n_{e0}$, $B(r)/B_0$ and $T_e(r)$ unchanged, as expressed in equation (28), is readily shown to follow from the fact that the dependence of ε on ω_p, ω_c and ω can be written (see for example equation (4))

$$\varepsilon = \varepsilon\left(\frac{\omega_p}{\omega}, \frac{\omega_c}{\omega}, \mu, T_e\right) . \tag{30}$$

In O–mode the reconstructed density profiles depend very little on the magnetic field and hence on η, except for the limitation that cyclotron absorption may impose on the spatial region over which the density profile can be probed. The graphs in figure 6 (a) therefore give a good estimate of the relativistic effects in O–mode for a wide range of plasma conditions.

In X–mode the relativistic effects vary significantly with η. Density profiles reconstructed with the cold model and normalized by n_{e0} are plotted in figure 7. Here the central temperature, T_{e0}, is kept constant at 10 keV while η is varied. With the major radius normalized by R_0 these curves cover a wide range of plasmas. For the cases covered in figure 7 the actual central density is at least 20 % greater than the peak reconstructed density. The depths to which the profiles with $\eta = 0.90$ and 0.60 can be reconstructed are limited by second harmonic cyclotron absorption in the outer region of the plasma. The depths to which the profiles could be probed were $R/R_0 = 1.04$ for $\eta = 0.90$ and $R/R_0 = 0.81$ for $\eta = 0.60$. The cold reconstruction overestimates this depth. In the cold plasma limit the X–mode radiation required to probe to the plasma centre and beyond will pass through the second harmonic cyclotron absorption layer if

$$\eta > \eta_0 = \frac{2(1 - a/R_0)}{(1 + a/R_0)^2} , \tag{31}$$

where a/R_0 is the inverse aspect ratio. For the plasmas considered in figure 7, $a/R_0 = 1/3$ giving $\eta_0 = 0.75$. The relativistic mass increase lowers the frequency at which cyclotron absorption sets in. This is counteracted by the relativistic lowering of the cutoff frequency. Equation (31) generally gives a good indication of when the centre of the plasma may be probed with X–mode, even when relativistic effects are taken into account.

At large values of ω_c^2/ω_p^2 the location of the cutoff is a weak function of density. In the cold plasma approximation and assuming that $B \propto 1/R$ a change, δR, in the location of the R cutoff results in a change, δn_e, in the cutoff density given by

$$\frac{\delta n_e}{n_e} = \frac{\omega_c^2}{\omega_p^2} \frac{\delta R}{R} . \tag{32}$$

This means that at low densities and high fields the reconstruction of density profiles from X–mode reflectometry becomes prone to noise. Some numerical noise is evident in the $\eta = 0.07$, 0.05 and 0.0033 curves in figure 7. It should be noted that numerical stability is not a problem at the values of η which are relevant for JET and other large Tokamaks.

In figure 8 reconstructed densities obtained for plasmas with a range of temperature profile shapes are given. P_T (see equation (14)) was varied while all other parameters were kept constant. Increasing P_T peaks up the temperature profile. It is evident that reconstruction based on the cold model underestimates the central density by an amount which is almost completely independent of the peaking of the temperature profile. The graphs in figure 8 further suggest that the depression in the cold reconstructed density profile at a given point depends on the temperature in the vicinity of that point and very little on the temperature in the rest of the plasma.

7 Conclusions

The dielectric properties of plasmas have been investigated for propagation perpendicular to the magnetic field at frequencies in the range of the electron cyclotron frequency and

the plasma frequency. Calculations of the Hermitian part of the dielectric tensor, refractive indices and locations of cutoffs based on cold, hot and relativistic plasma models were compared. While only small differences were found between the cold and the hot models, substantial differences in all three quantities were found between the cold and hot predictions on the one hand and the relativistic on the other. The differences are larger than a simple comparison of T_e with $m_e c^2$ might suggest.

Cold and relativistic predictions for reflectometry were compared. It was found that relativistic effects are of practical importance for X–mode reflectometry in large Tokamaks, because (a) cold analysis leads to a considerable underestimation of the electron density profile and (b) the location of the cutoff may be shifted by a significant fraction of the minor radius. (a) implies that for density profile measurements using X–mode reflectometry (an attractive option for ITER) the data must be analysed with a relativistic plasma model. (b) has consequences for the determination of where fluctuations observed with correlation reflectometry are situated in the plasma.

While the relativistic modifications found in O–mode are smaller than in X–mode they may still have to be taken into account, except near the plasma edge. For typical JET parameters the relativistic shifts of density profiles derived from O–mode reflectometery can be of the same order or larger than the estimated non–relativistic errors on density profiles obtained with the JET O–mode multichannel reflectometer. This diagnostic will therefore benefit from a data analysis which takes relativistic effects into account.

A code for relativistic reconstruction of the electron density profile from the phase shift function has been written and tested with simulated reflectometric data.

Simple and accurate approximations have been found for the relativistic O–mode refractive index and for the relation between density and frequency at the O–mode cutoff. These approximations permit accurate reconstruction of density profiles from simulated O–mode reflectometry.

8 Acknowledgements

Useful discussions with A.C.C. Sips on the performance of the JET multichannel reflectometer and helpful comments from A.E. Costley and T.P. Hughes are gratefully acknowledged.

References

BATCHELOR D. B., GOLDFINGER R. C. and WEITZNER H. (1984) *Phys. Fluids*, **27**, 2835.

BINDSLEV H. (1991a) *Plasma Physics and Controlled Fusion*, **33**, 1775.

BINDSLEV H. (1991b) Proc. 18^{th} EPS Conference on Controlled Fusion and Plasma Physics, 15C, part IV, p. 9, Berlin.

BINDSLEV H. (1991c) Proc. The International School of Plasma Physics "Piero Caldirola", p. 779, Varenna.

BORNATICI M., CANO R, DE BARBIERI O. and ENGELMANN F. (1983) *Nuclear Fusion*, **23**, 1153.

COSTLEY A.E., CRIPWELL P., PRENTICE R. and SIPS A.C.C. (1990) *Rev. Sci. Instrum.*, **61**, 2823.

COSTLEY A.E. (1991) Proc. The International School of Plasma Physics "Piero Caldirola", p. 113, Varenna.

CRIPWELL P., COSTLEY A.E. and HUBBARD A.E. (1989) Proc. 16^{th} EPS Conference on Controlled Fusion and Plasma Physics, 13B, part I, p. 75, Venice.

CRIPWELL P. and COSTLEY A.E. (1991) Proc. 18^{th} EPS Conference on Controlled Fusion and Plasma Physics, 15C, part I, p. 17, Berlin.

DOYLE E.J., LEHECKA T., LUHMANN N.C. and PEEBLES W.A. (1990) Proc. 17^{th} EPS Conference on Controlled Fusion and Plasma Heating, 14B, part IV, p. 1596, Amsterdam.

GINZBURG V.L. (1970), *The Propagation of Electromagnetic Waves in Plasmas* , 2^{nd} edition, §30. Pergamon Press, Oxford.

MANSO M.E., WAGNER F., MATIAS J., SILVA A., ZOHM H., SERRA F., BÜCHSE R. and VARELA P. (1991) Proc. 18^{th} EPS Conference on Controlled Fusion and Plasma Physics, 15C, part I, p. 393, Berlin.

MAZZUCATO E. and NAZIKIAN R. (1991) *Plasma Physics and Controlled Fusion*, **33**, 261.

PAVLICHENKO O. and SKIBENKO A. (1989), ITER ref. doc. ITER–IL–PH–7–9–S–4.

PRENTICE R., SIPS A.C.C., FESSEY J.A. and COSTLEY A.E. (1990) Proc. 17^{th} EPS Conference on Controlled Fusion and Plasma Heating, 14B, part IV, p. 1500, Amsterdam.

SHKAROFSKY I. P. (1986) *J. Plasma Physics*, **35**, 319.

SIPS A.C.C. (1991), PhD thesis, Eindhoven University of Technology.

SIPS A.C.C. (1992), private communication.

SWANSON D. G. (1989), *Plasma Waves.* Academic Press, Boston.

TRUBNIKOV B. A. (1959), in *Plasma Physics and the Problem of Controlled Thermonuclear Reactions* (ed. LEONTOVICH M. A.). Vol. 3, Pergamon Press, London, 122.

ZOU X. L., LAURENT L. and RAX J.M. (1991) *Plasma Physics and Controlled Fusion*, **33**, 903.

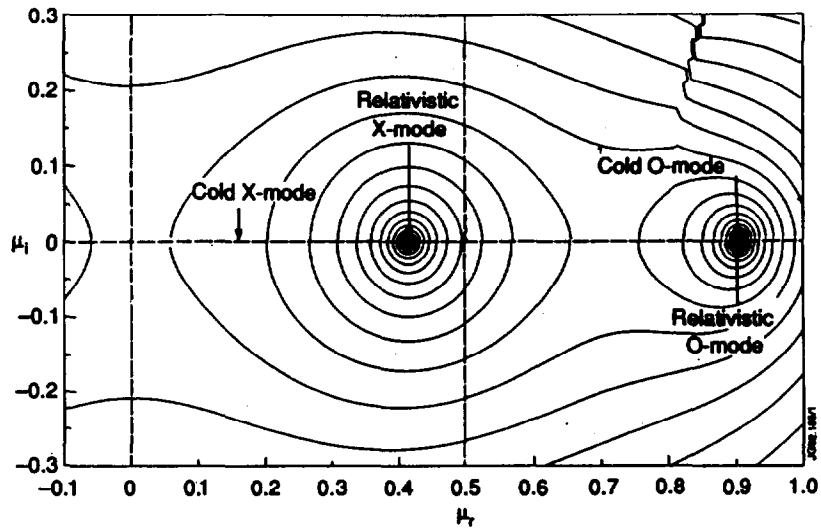

Figure 1: Contour plots of the logarithm of the weakly relativistic plasma dispersion function, $\log(|\Lambda|)$, in the complex μ plane. The weakly relativistic modes appear as singularities in this plot. The cold O- and X-mode refractive indices are also indicated. Parameters: $T_e = 15$ keV, $n_e = 6.0 \cdot 10^{19}\, m^{-3}$, $B = 3.0$ T, $\angle(\mathbf{B},\mathbf{k}) = 90°$, $f = 124$ GHz. ($f_{ce} \approx 84$ GHz, $f_p \approx 70$ GHz, $f_R \approx 123$ GHz)

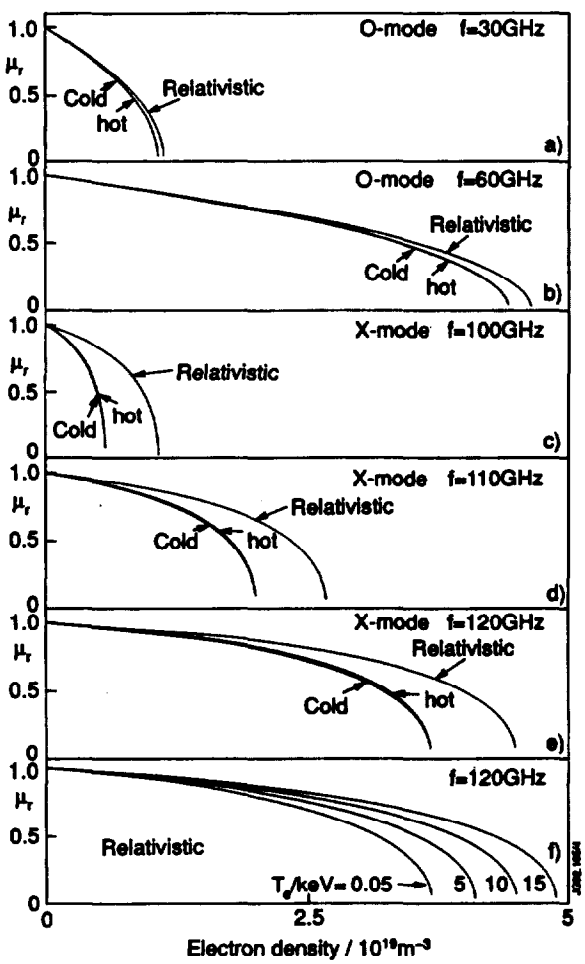

Figure 2: Refractive index, μ, as a function of electron density. Parameters:
B = 3.4 T, $\angle$ (B,k) = 90°.
(a)-(e) cold, hot and weakly relativistic, $T_e = 10$ keV,
(a) O-mode, $f = 30$ GHz,
(b) O-mode, $f = 60$ GHz,
(c) X-mode, $f = 100$ GHz,
(d) X-mode, $f = 110$ GHz,
(e) X-mode, $f = 120$ GHz.
(f) weakly relativistic,
$T_e = 0.05, 5, 10, 15$ keV,
X-mode, $f = 120$ GHz

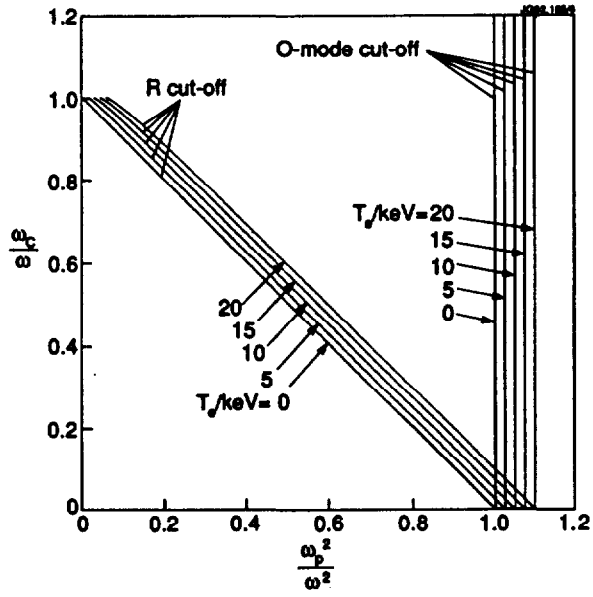

Figure 3: Locations of the R cutoff and O–mode cutoff predicted by the fully relativistic plasma model, plotted in an ω_c/ω versus ω_p^2/ω^2 diagram (CMA diagram). T_e = 0.1, 5, 10, 15, 20 keV. The T_e = 0.1 keV curves are almost identical to the cold curves.

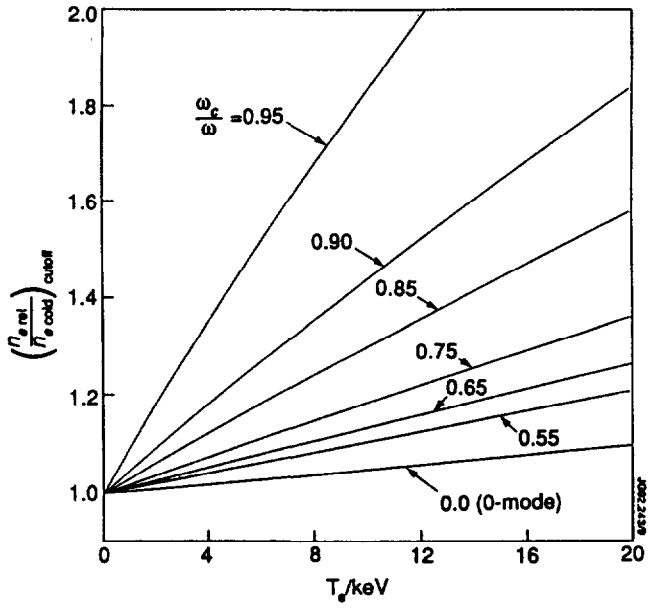

Figure 4: Cutoff densities predicted by the fully relativistic plasma model and normalized by the equivalent cutoff densities found with the cold theory as functions of temperature. Curves are given for O–mode and for X–mode with a range of values of ω_c/ω. The X–mode curve with $\omega_c/\omega = 0$ is identical to the O–mode curve.

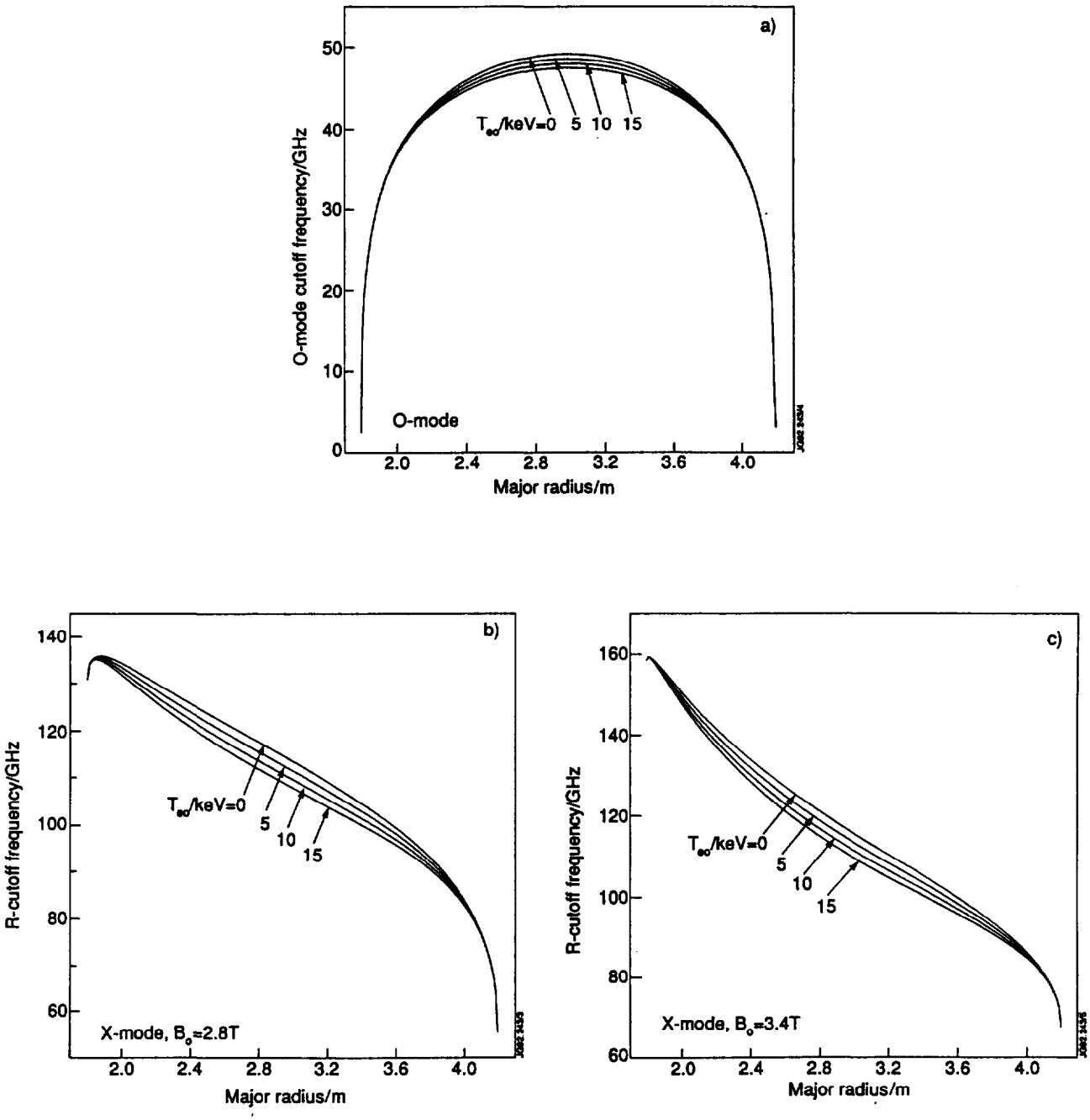

Figure 5: Cutoff frequency as a function of major radius. Plasma profiles are defined in equations (14)–(16). Parameters: $R_0 = 3$ m, $a = 1.2$ m, $p_n = 0.5$, $n_{el} = 1 \cdot 10^{17}\mathrm{m}^{-3}$, $T_{e0} = 0.1, 5.1, 10.1, 15.1$ keV, $p_T = 1$, $T_{el} = 100$ eV, (a) O–mode, $B_0 = 3.4$ T, $n_{e0} = 3.01 \cdot 10^{19}\mathrm{m}^{-3}$, (b) X–mode, $B_0 = 2.8$ T, $n_{e0} = 5.01 \cdot 10^{19}\mathrm{m}^{-3}$, (c) X–mode, $B_0 = 3.4$ T, $n_{e0} = 3.01 \cdot 10^{19}\mathrm{m}^{-3}$.

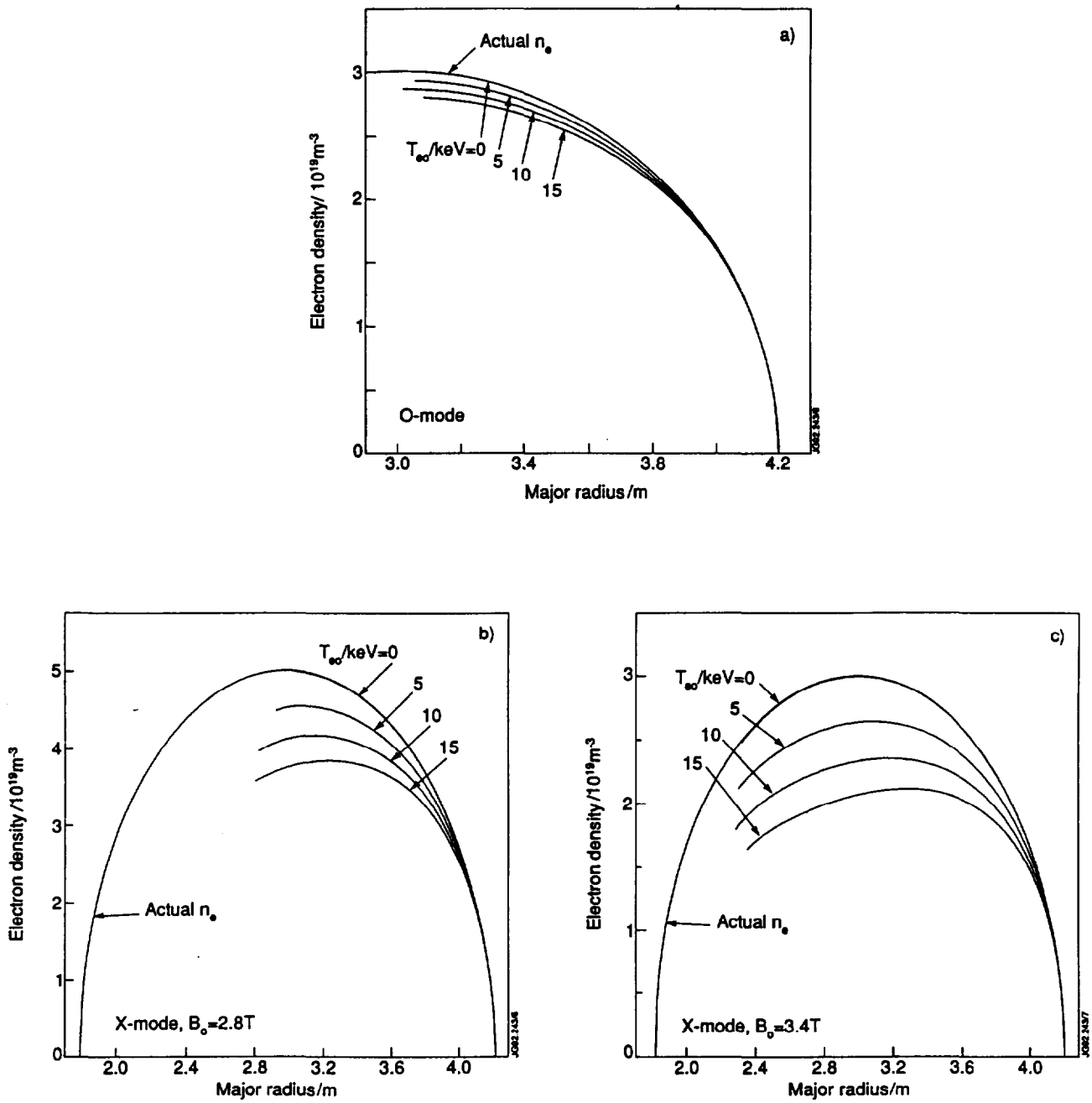

Figure 6: Actual electron density profile and reconstructed density profiles derived using the cold plasma model for analysing phase functions, $\Psi(\omega)$, obtained with the relativistic model. Plasma profiles are defined in equations (14)–(16). Parameters: (identical to those used in figure 5) $R_0 = 3$ m, $a = 1.2$ m, $p_n = 0.5$, $n_{el} = 1 \cdot 10^{17}\mathrm{m}^{-3}$, $T_{e0} = 0.1$, 5.1, 10.1, 15.1 keV, $p_T = 1$, $T_{el} = 100$ eV, (a) O–mode, $B_0 = 3.4$ T, $n_{e0} = 3.01 \cdot 10^{19}\mathrm{m}^{-3}$, (b) X–mode, $B_0 = 2.8$ T, $n_{e0} = 5.01 \cdot 10^{19}\mathrm{m}^{-3}$, (c) X–mode, $B_0 = 3.4$ T, $n_{e0} = 3.01 \cdot 10^{19}\mathrm{m}^{-3}$. For X–mode the maximum probing frequency and hence the maximum depth to which the density profiles can be reconstructed is limited by absorption in the outer region of the plasma at the second harmonic of the cyclotron frequency.

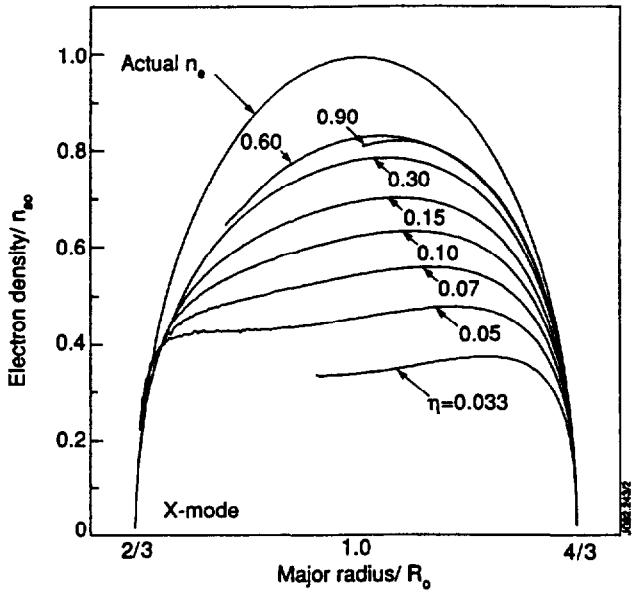

Figure 7: As figure 6 but with parameters: $R_0/a = 3$, $p_n = 0.5$, $n_{el}/n_{e0} = 1/100$, $\eta = 0.90$, 0.60, 0.30, 0.10, 0.07, 0.05, 0.033, $T_{e0} = 10.1$ keV, $p_T = 1$, $T_{el} = 100$ eV, X–mode. For $\eta = 0.90$ and 0.60 the maximum probing frequency and hence the maximum depth to which the density profiles can be reconstructed is limited by absorption in the outer region of the plasma at the second harmonic of the cyclotron frequency. For $\eta = 0.033$ the depth is limited by numerical noise in the reconstruction.

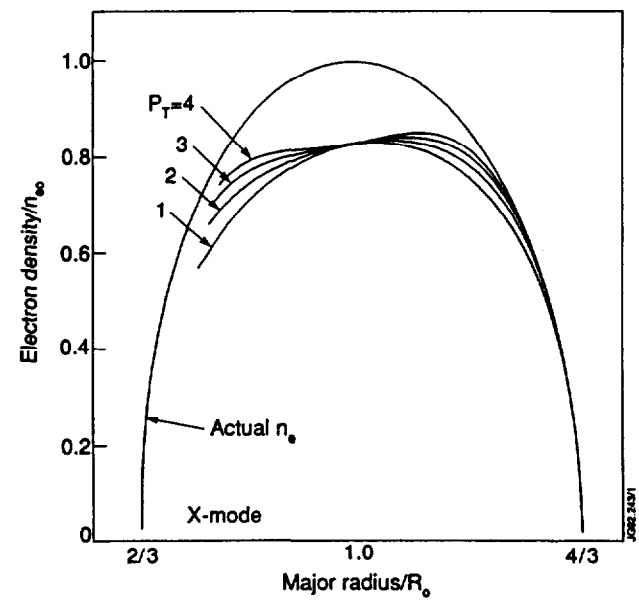

Figure 8: As figure 6 but with parameters: $R_0/a = 3$, $p_n = 0.5$, $n_{el}/n_{e0} = 1/100$, $\eta = 0.5$, $T_{e0} = 10.1$ keV, $p_T = 1$, 2, 3, 4, $T_{el} = 100$ eV, X–mode. The maximum probing frequency and hence the maximum depth to which the density profiles can be reconstructed is limited by absorption in the outer region of the plasma at the second harmonic of the cyclotron frequency.

ANNEX

P.-H. REBUT, A. GIBSON, M. HUGUET, J.M. ADAMS[1], B. ALPER, H. ALTMANN, A. ANDERSEN[2], P. ANDREW[3], M. ANGELONE[4], S. ALI-ARSHAD, P. BAIGGER, W. BAILEY, B. BALET, P. BARABASCHI, P. BARKER, R. BARNSLEY[5], M. BARONIAN, D.V. BARTLETT, L. BAYLOR[6], A.C. BELL, G. BENALI, P. BERTOLDI, E. BERTOLINI, V. BHATNAGAR, A.J. BICKLEY, D. BINDER, H. BINDSLEV[2], T. BONICELLI, S.J. BOOTH, G. BOSIA, M. BOTMAN, D. BOUCHER, P. BOUCQUEY, P. BREGER, H. BRELEN, H. BRINKSCHULTE, D. BROOKS, A. BROWN, T. BROWN, M. BRUSATI, S. BRYAN, J. BRZOZOWSKI[7], R. BUCHSE[22], T. BUDD, M. BURES, T. BUSINARO, P. BUTCHER, H. BUTTGEREIT, C. CALDWELL-NICHOLS, D.J. CAMPBELL, P. CARD, G. CELENTANO, C.D. CHALLIS, A.V. CHANKIN[8], A. CHERUBINI, D. CHIRON, J. CHRISTIANSEN, P. CHUILON, R. CLAESEN, S. CLEMENT, E. CLIPSHAM, J.P. COAD, I.H. COFFEY[9], A. COLTON, M. COMISKEY[10], S. CONROY, M. COOKE, D. COOPER, S. COOPER, J.G. CORDEY, W. CORE, G. CORRIGAN, S. CORTI, A.E. COSTLEY, G. COTTRELL, M. COX[11], P. CRIPWELL[12], O. Da COSTA, J. DAVIES, N. DAVIES, H. de BLANK, H. de ESCH, L. de KOCK, E. DEKSNIS, F. DELVART, G.B. DENNE-HINNOV, G. DESCHAMPS, W.J. DICKSON[13], K.J. DIETZ, S.L. DMITRENKO, M. DMITRIEVA[14], J. DOBBING, A. DOGLIO, N. DOLGETTA, S.E. DORLING. P.G. DOYLE, D.F. DÜCHS, H. DUQUENOY, A. EDWARDS, J. EHRENBERG, A. EKEDAHL, T. ELEVANT[7], S.K. ERENTS[11], L.G. ERIKSSON, H. FAJEMIROKUN[12], H. FALTER, J. FREILING[15], F. FREVILLE, C. FROGER, P. FROISSARD, K. FULLARD, M. GADEBERG, A. GALETSAS, T. GALLAGHER, D. GAMBIER, M. GARRIBBA, P. GAZE, R. GIANNELLA, R.D. GILL, A GIRARD, A. GONDHALEKAR, D. GOODALL[11], C. GORMEZANO, N.A. GOTTARDI, C. GOWERS, B.J. GREEN, B. GRIEVSON, R. HAANGE, A. HAIGH, C.J. HANCOCK, P.J. HARBOUR, T. HARTRAMPF, N.C. HAWKES[11], P. HAYNES[11], J.L. HEMMERICH, T. HENDER[11], J. HOEKZEMA, D. HOLLAND, M. HONE, L. HORTON, J. HOW, M. HUART, I. HUGHES, T.P. HUGHES[10], M. HUGON, Y. HUO[16], K. IDA[17], B. INGRAM, M. IRVING, J. JACQUINOT, H. JAECKEL, J.F. JAEGER, G. JANESCHITZ, Z. JANKOVICZ[18], O.N. JARVIS, F. JENSEN, E.M. JONES, H.D. JONES, L.P.D.F. JONES, S. JONES[19], T.T.C. JONES, J.-F. JUNGER, F. JUNIQUE, A. KAYE, B.E. KEEN, M. KEILHACKER, G.J. KELLY, W. KERNER, A. KHUDOLEEV[21], R. KONIG, A. KONSTANTELLOS, M. KOVANEN[20], G. KRAMER[15], P. KUPSCHUS, R. LÄSSER, J.R. LAST, B. LAUNDY, L. LAURO-TARONI, M. LAVEYRY, K. LAWSON[11], M. LENNHOLM, J. LINGERTAT[22], R.N. LITUNOVSKI, A. LOARTE, R. LOBEL, P. LOMAS, M. LOUGHLIN, C. LOWRY, J. LUPO, A.C. MAAS[15], J. MACHUZAK[19], B. MACKLIN, G. MADDISON[11], C.F. MAGGI[23], G. MAGYAR, W. MANDL[22], V. MARCHESE, G. MARCON, F. MARCUS, J. MART, D. MARTIN, E. MARTIN, R. MARTIN-SOLIS[24], P. MASSMANN, G. MATTHEWS, H. McBRYAN, G. McCRACKEN[11], J. McKIVITT, P. MERIGUET, P. MIELE, A. MILLER, J. MILLS, S.F. MILLS, P. MILLWARD, P. MILVERTON, E. MINARDI[4], R. MOHANTI[25], P.L. MONDINO, D. MONTGOMERY[26], A. MONTVAI[27], P. MORGAN, H. MORSI, D. MUIR, G. MURPHY, R. MYRNÄS[28], F. NAVE[29], G. NEWBERT, M. NEWMAN, P. NIELSEN, P. NOLL, W. OBERT, D. O'BRIEN, J. ORCHARD, J. O'ROURKE, R. OSTROM, M. OTTAVIANI, M. PAIN, F. PAOLETTI, S. PAPASTERGIOU, W. PARSONS, D. PASINI, D. PATEL, A. PEACOCK, N. PEACOCK[11], R.J.M. PEARCE, D. PEARSON[12], J.F. PENG[16], R. PEPE DE SILVA, G. PERINIC, C. PERRY, M. PETROV[21], M.A. PICK, J. PLANCOULAINE, J.-P POFFÉ, R. PÖHLCHEN, F. PORCELLI, L. PORTE[13], R. PRENTICE, S. PUPPIN, S. PUTVINSKII[8], G. RADFORD[30], T. RAIMONDI, M.C. RAMOS DE ANDRADE, R. REICHLE, J. REID, S. RICHARDS, E. RIGHI, F. RIMINI, D. ROBINSON[11], A. ROLFE, R.T. ROSS, L. ROSSI, R. RUSS, P. RUTTER, H.C. SACK, G. SADLER, G. SAIBENE, J.L. SALANAVE, G. SANAZZARO, A. SANTAGIUSTINA, R. SARTORI, C. SBORCHIA, P. SCHILD, M. SCHMID, G. SCHMIDT[31], B. SCHUNKE, S.M. SCOTT, L. SERIO, A SIBLEY, R. SIMONINI, A.C.C. SIPS, P. SMEULDERS, R. SMITH, R. STAGG, M. STAMP, P. STANGEBY[3], R. STANKIEWICZ[32], D.F. START, C.A. STEED, D. STORK, P.E. STOTT, P. STUBBERFIELD, D. SUMMERS, H. SUMMERS[13], L. SVENSSON, J.A. TAGLE[33], M. TALBOT, A. TANGA, A. TARONI, C. TERELLA, A TERRINGTON, A TESINI, P.R. THOMAS, E. THOMPSON, K. THOMSEN, F. TIBONE, A. TISCORNIA, P. TREVALION, B. TUBBING, P. VAN BELLE, H. VAN DER BEKEN, G. VLASES, M. VON HELLERMANN, T. WADE, C. WALKER, R. WALTON[31], D. WARD, M.L. WATKINS, N. WATKINS, M.J. WATSON, S. WEBER[34], J. WESSON, T.J. WIJNANDS, J. WILKS, D. WILSON, T. WINKEL, R. WOLF, D. WONG, C. WOODWARD, Y. WU[35], M. WYKES, D. YOUNG, I.D. YOUNG, L. ZANNELLI, A. ZOLFAGHARI[19], W. ZWINGMANN

[1] Harwell Laboratory, UKAEA, Harwell, Didcot, Oxfordshire, UK.
[2] Risø National Laboratory, Roskilde, Denmark.
[3] Institute for Aerospace Studies, University of Toronto, Downsview, Ontario, Canada.
[4] ENEA Frascati Energy Research Centre, Frascati, Rome, Italy.
[5] University of Leicester, Leicester, UK.
[6] Oak Ridge National Laboratory, Oak Ridge, TN, USA.
[7] Royal Institute of Technology, Stockholm, Sweden.
[8] I.V. Kurchatov Institute of Atomic Energy, Moscow, Russian Federation.
[9] Queens University, Belfast, UK.
[10] University of Essex, Colchester, UK.
[11] Culham Laboratory, UKAEA, Abingdon, Oxfordshire, UK.
[12] Imperial College of Science, Technology and Medicine, University of London, London, UK.
[13] University of Strathclyde, Glasgow, UK.
[14] Keldysh Institute of Applied Mathematics, Moscow, Russian Federation.
[15] FOM-Institute for Plasma Physics "Rijnhuizen", Nieuwegein, Netherlands.
[16] Institute of Plasma Physics, Academia Sinica, Hefei, Anhui Province, China.
[17] National Institute for Fusion Science, Nagoya, Japan.
[18] Soltan Institute for Nuclear Studies, Otwock/Świerk, Poland.
[19] Plasma Fusion Center, Massachusetts Institute of Technology, Boston, MA, USA.
[20] Nuclear Engineering Laboratory, Lappeenranta University, Finland.
[21] A.F. Ioffe Physico-Technical Institute, St. Petersburg, Russian Federation.
[22] Max-Planck-Institut für Plasmaphysik, Garching, Germany.
[23] Department of Physics, University of Milan, Milan, Italy.
[24] Universidad Complutense de Madrid, Madrid, Spain.
[25] North Carolina State University, Raleigh, NC, USA.
[26] Dartmouth College, Hanover, NH, USA.
[27] Central Research Institute for Physics, Budapest, Hungary.
[28] University of Lund, Lund, Sweden.
[29] Laboratorio Nacional de Engenharia e Tecnologia Industrial, Sacavem, Portugal.
[30] Institute of Mathematics, University of Oxford, Oxford, UK.
[31] Princeton Plasma Physics Laboratory, Princeton University, Princeton, NJ, USA.
[32] RCC Cyfronet, Otwock/Świerk, Poland,
[33] Centro de Investigaciones Energéticas, Medioambientales y Tecnológicas, Madrid, Spain.
[34] Freie Universität, Berlin, Germany.
[35] Insitute for Mechanics, Academia Sinica, Beijing, China.